Scaleup of laboratory data for surfactant-alternating-gas foam enhanced oil recovery

Salazar-Castillo, Rodrigo O.; Rossen, William R.

DOI
10.2118/201204-PA

Publication date
2020

Document Version
Final published version

Published in
SPE Journal

Scaleup of Laboratory Data for Surfactant-Alternating-Gas Foam Enhanced Oil Recovery

Rodrigo O. Salazar-Castillo and **William R. Rossen,** Delft University of Technology

Summary

Foam increases sweep efficiency during gas injection in enhanced oil recovery processes. Surfactant alternating gas (SAG) is the preferred method to inject foam for both operational and injectivity reasons. Dynamic SAG corefloods are unreliable for direct scaleup to the field because of core-scale artifacts. In this study, we report fit and scaleup local-equilibrium (LE) data at very-low injected-liquid fractions in a Bentheimer core for different surfactant concentrations and total superficial velocities.

We fit LE data to an implicit-texture foam model for scaleup to a dynamic foam process on the field scale using fractional-flow theory. We apply different parameter-fitting methods (least-squares fit to entire foam-quality scan and the method of Rossen and Boeije 2015) and compare their fits to data and predictions for scaleup. We also test the implications of complete foam collapse at irreducible water saturation for injectivity.

Each set of data predicts a shock front with sufficient mobility control at the leading edge of the foam bank. Mobility control improves with increasing surfactant concentration. In every case, scaleup injectivity is much better than with coinjection of gas and liquid. The results also illustrate how the foam model without the constraint of foam collapse at irreducible water saturation (Namdar Zanganeh et al. 2014) can greatly underestimate injectivity for strong foams.

For the first time, we examine how the method of fitting the parameters to coreflood data affects the resulting scaleup to field behavior. The method of Rossen and Boeije (2015) does not give a unique parameter fit, but the predicted mobility at the foam front is roughly the same in all cases. However, predicted injectivity does vary somewhat among the parameter fits. Gas injection in a SAG process depends especially on behavior at low injected-water fraction and whether foam collapses at the irreducible water saturation, which may not be apparent from a conventional scan of foam mobility as a function of gas fraction in the injected foam. In two of the five cases examined, this method of fitting the whole scan gives a poor fit for the shock in gas injection in SAG. We also test the sensitivity of the scaleup to the relative permeability $k_{rw}(S_w)$ function assumed in the fit to data.

There are many issues involved in scaleup of laboratory data to field performance: reservoir heterogeneity, gravity, interactions between foam and oil, and so on. This study addresses the best way to fit model parameters without oil for a given permeability, an essential first step in scaleup before considering these additional complications.

Introduction

After primary production of oil, gas may be injected into the reservoir. Under ideal conditions, gas is able to displace virtually all of the remaining oil, as long as the injected gas contacts the residing oil (Lake et al. 2014). However, geological heterogeneity and gravity segregation cause gas to migrate to high-permeability layers and to the top of the reservoir. Low gas viscosity compounds these effects. Foam is able to divert flow from high-permeability layers to low-permeability layers (Schramm 1994; Rossen 1996). Foam is able to reduce gravity segregation by reducing gas mobility. These combined properties increase gas's sweep efficiency and result in an attractive enhanced-oil-recovery method.

For operational and sweep-efficiency reasons, the best method of injection of foam is usually a SAG (also called FAWAG) (Matthews 1989; Heller 1994; Shan and Rossen 2004). During a SAG process, foam is formed away from the injection well, thus offering better injectivity than a coinjection process (Al Ayesh et al. 2017). Also, SAG is uniquely suited to overcoming gravity override (Kloet et al. 2009; De Velde Harsenhorst et al. 2013; Boeije and Rossen 2015b).

Scaling up laboratory results to the field scale remains a challenge (Rossen and Boeije 2015). One approach involves dynamic coreflood experiments where gas is injected into a fully surfactant-saturated core. These experiments often do not reach LE during the injection of the first pore volume (PV) of gas (Kapetas et al. 2014). This failure to reach LE on the laboratory scale can greatly distort the interpretation of the data in terms of LE-foam models. Other effects, such as the entrance region and dispersion, could also distort laboratory-scale experiments.

At the field scale, foam models generally assume that LE applies. Therefore, steady-state corefloods are a feasible alternative approach to dynamic experiments. According to fractional-flow theory, during gas injection in SAG, the mobility of the foam bank depends on the fractional-flow curve $f_w(S_w)$ at extremely low liquid fraction f_w (Zhou and Rossen 1995; Shan and Rossen 2004). Consequently, some studies have aimed to scale up a gas-injection process during a SAG by focusing on steady-state experiments in this region of the $f_w(S_w)$ curve (Kibodeaux and Rossen 1997; Xu and Rossen 2004; Boeije and Rossen 2018).

Fig. 1 depicts a gas-injection process, specifically injection of the first gas slug into a surfactant-saturated reservoir. The initial, *I,* and injection, *J,* conditions correspond to water saturation $S_w = 1$ and water fractional flow $f_w = 0$, respectively. Note that the abrupt increase in foam mobility at a distinctive water saturation, S_w*, imposed by the limiting capillary pressure (Khatib et al. 1988), results in a steep fractional-flow curve $f_w(S_w)$ near S_w* (Zhou and Rossen 1995). The resulting fractional-flow curve does not have a path from *I* to *J* with monotonically increasing slope df_w/dS_w. Therefore, the portion of the path connecting *I* to a point of tangency must be replaced by a shock or discontinuity. After the shock, a spreading wave connects the point of tangency and *J*.

The dimensionless time-distance diagram for the injection of the first gas slug in SAG is illustrated on the right of Fig. 1. The mobilities of the shock and of the characteristics continuously increase as one approaches the injection well at dimensionless position $x_D = 0$ at any given dimensionless time t_D. The mobility at the shock is crucial to maintaining viscous stability during the foam displacement. Only relatively low mobility behind the shock can provide a stable front.

Original SPE manuscript received for review 8 October 2019. Revised manuscript received for review 17 February 2020. Paper (SPE 201204) peer approved 5 March 2020.

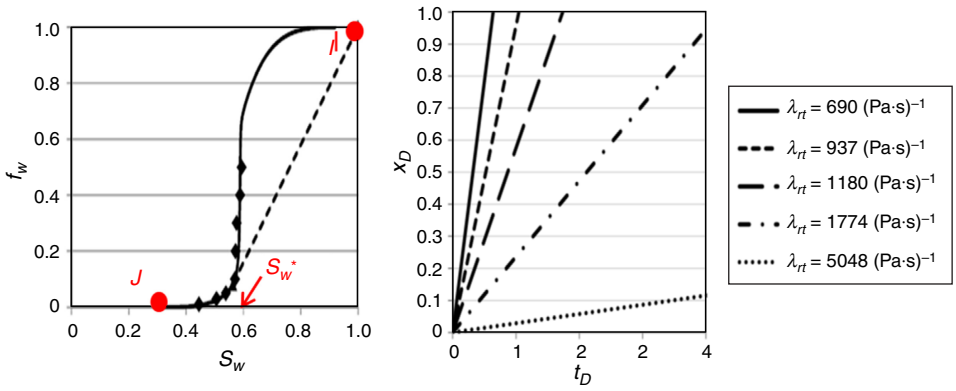

Fig. 1—(Left) Fractional-flow curve adapted from Boeije and Rossen (2018). The red dots denote the initial (I) and injection (J) conditions for injection of the first gas slug. (Right) Dimensionless time-distance diagram for the corresponding gas-injection process (Boeije and Rossen 2018). The mobilities of the shock, solid line, and four of the characteristics, represented as dotted lines, are included.

Another complication in laboratory-foam corefloods is the capillary end effect at the core outlet, where foam generation occurs because of higher water saturation there (Ransohoff and Radke 1988). Experimental studies (Apaydin and Kovscek 2001; Nguyen et al. 2003; Simjoo et al. 2013) have reported an eruption of a much-stronger foam at the core outlet and subsequent, slow upstream propagation of a stronger-foam state. Apaydin and Kovscek (2001) observed this behavior at relatively high surfactant concentrations. They claim it is initiated by the capillary end effect, and upstream propagation of the foam front reflects greater gas trapping just upstream of the foam. However, the mechanism for this increased trapping is not specified. Moreover, estimation of gas trapping in coreflood experiments (Nguyen et al. 2009) is difficult. Thus, there is still no complete explanation for the upstream propagation of this stronger-foam state. Nevertheless, the eruption of a much-stronger foam depends on behavior near the core outlet; its relevance to a foam process in a homogenous reservoir at the field scale is dubious, and its relevance to heterogeneous reservoirs is unclear.

Several previous studies have found fractional-flow curves $f_w(S_w)$ that are nonmonotonic in S_w. **Fig. 2** illustrates how, in these cases, the fractional-flow curve, $f_w(S_w)$, shifts to higher S_w as f_w decreases. Then, S_w decreases again on further decrease in f_w. In fact, about half of the published examples from laboratory LE studies are not monotonic (Kibodeaux and Rossen 1997; Wassmuth et al. 2001; Xu and Rossen 2004; Boeije and Rossen 2018). Rossen and Bruining (2007) show that this behavior, scaled up to the field, indicates to a shock to complete foam collapse and therefore failure of mobility control at the leading edge of the foam bank, as illustrated in Fig. 2.

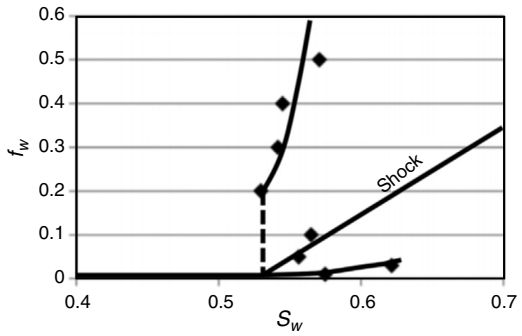

Fig. 2—Shock construction for the injection of the first gas slug in a SAG for a multivalued fractional-flow curve (Boeije and Rossen 2018).

In this paper, we present a variety of data sets that follow the monotonic pattern, as in Fig. 1. Each data set consists of a foam scan (i.e., foam mobility as a function of fractional flow f_w). From foam mobility, we estimate water saturation assuming a water relative-permeability function $k_{rw}(S_w)$. We examine the effects of surfactant concentration and total superficial velocity on the fractional-flow curve $f_w(S_w)$. We fit the data to foam-model parameters using the conventional method of a least-squares fit to the entire foam scan (Eftekhari and Farajzadeh 2017; Kapetas et al. 2017) and the method of Rossen and Boeije (2015) for a SAG, which focuses on fitting the data in the low range of f_w. We do the scaleup with the parameters determined from the model fits and calculate the mobility at the shock for a hypothetical field application. The method of Rossen and Boeije (2015) does not guarantee a unique parameter fit. We present a range of possible reasonable fits to the data using this method and indicate the corresponding range of differences in the scaleup. We compare the mobilities at the shock predicted by both fitting methods and illustrate how the injection strategy impacts the most suitable fitting method. We test the impact of complete foam collapse at the residual water saturation on the obtained parameters and on the injectivity by incorporating the Namdar Zanganeh correction (2014). Finally, we test the sensitivity of the fit to the $k_{rw}(S_w)$ function assumed on the scaled up behavior for one of our experiments.

A companion paper (Salazar and Rossen 2019; see also Salazar Castillo 2019) examines cases where we see nonmonotonic behavior, as depicted in Fig. 2. In that paper, we discuss what characterizes those cases and whether they reflect a laboratory artifact or would scale up to failure in the field. In this study, we do not address liquid injectivity in SAG, except as it may be affected by foam collapse during injection of gas. Gong et al. (2019) discuss the effect of gas injection on subsequent liquid injectivity.

Experimental Apparatus

We conducted coreflood experiments in two setups: A and B. Apparatus A, depicted in **Fig. 3,** is able to coinject gas (nitrogen) and surfactant solution over a range of total superficial velocities between 0.82 and 16 ft/D. We injected the liquid phase using a Vindum pump model VP1 (Vindum Engineering, Inc., Lodi, California, USA), which is able to deliver a minimum flow rate accurately as low as 1×10^{-4} mL/min. To inject the gas phase, we used a Bronkhorst® gas mass-flow controller Model F-033CI (Bronkhorst High-Tech B.V., Ruurlo, The Netherlands) that, in combination with a Coriolis flowmeter, is able to deliver a flow rate between 1.2 and 60 g/h (0.49 and 22.40 mL/min nitrogen at 40 bar pressure and 30°C temperature). A glued core is placed into a polyether ether ketone core holder with a narrow liquid-filled gap in between, pressurized to the injection pressure. We placed the core holder vertically, and we injected the fluids from bottom to top. To help achieve local equilibrium, in some cases (as described in the Experimental Procedure section and Appendix A), we used a foam generator upstream of the core inlet: a polyether ether ketone three-way connector with a built-in micrometric filter. To limit gas expansion along the core, a backpressure regulator fixed at either 40 or 80 bar was placed at the outlet of the core. Backpressure was held constant during each experiment. The magnitude of backpressure was selected to allow the mass-flow controller to deliver gas over the range of volumetric injection rates corresponding to the superficial velocity and range of foam qualities for the given experiment. The velocity and foam quality were calculated by applying the Jacobsen-Stewart equation of state (Jacobsen and Stewart 1973).

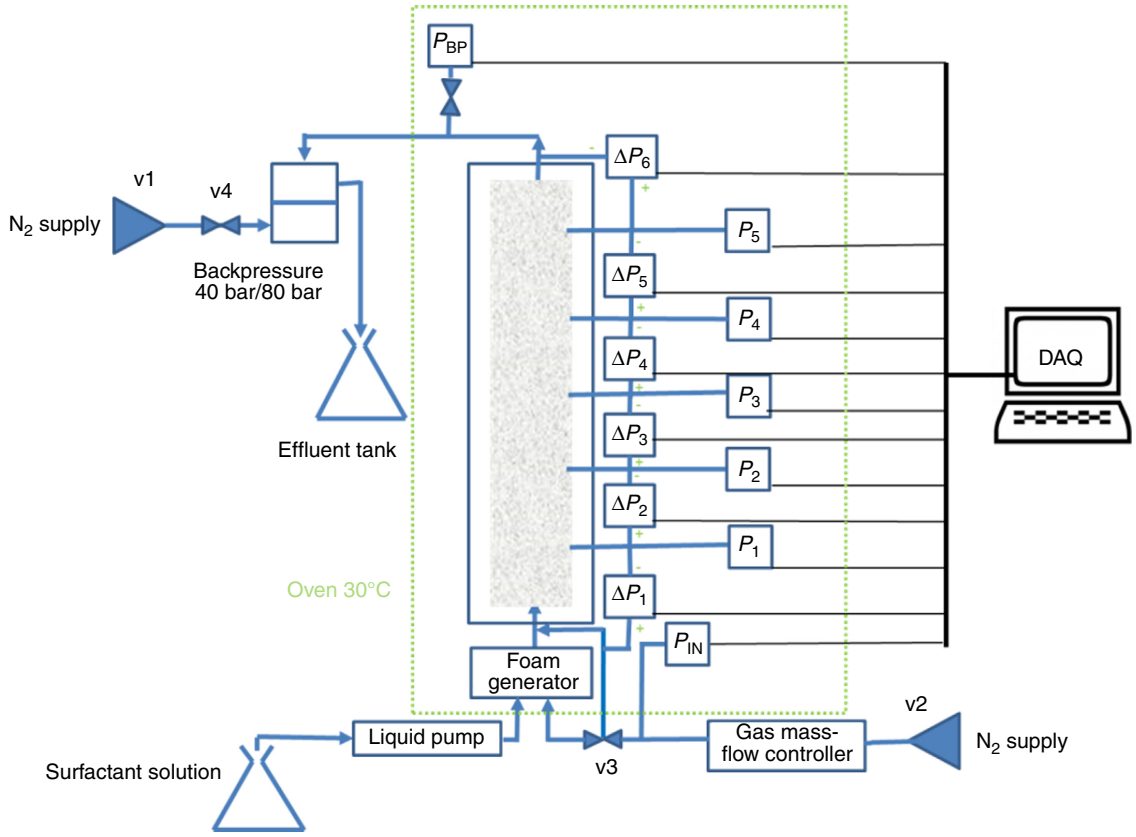

Fig. 3—Experimental Apparatus A, with controlled temperature. Apparatus B is substantially similar, with changes noted in the text. DAQ = data acquisition; N_2 = nitrogen.

Seven absolute-pressure transducers and six differential-pressure transducers were connected using lines filled with liquid, connected to the core, to monitor gas expansion and foam mobility along the core. The setup was placed inside an oven maintained at 30°C. Apparatus B is an adaptation of apparatus A to fit in an X-ray computed tomography (CT) scanner to monitor water saturation during corefloods. The core holder was place horizontally in the CT scanner because it would not fit in the scanner if held vertically. Polyether ether ketone lines replaced the metal lines connected to the core holder to reduce the X-ray attenuation. In both setups, we digitally recorded the pressure and temperature data every 1.7 seconds using a program coded in the language LabVIEW (National Instruments, Austin, Texas, USA).

Materials

During the coreflood experiments, we coinjected nitrogen and surfactant solution to generate foam. The nitrogen was supplied by a 200-bar cylinder with a purity of 99.98%. The surfactant solutions consisted of a synthetic brine prepared with demineralized water, 1.0 wt% sodium chloride, and anionic alpha olefin sulfonate (AOS) surfactant (BIO-TERGE® AS-40; Stepan Company, Northfield, Illinois, USA). We prepared four formulations with surfactant concentrations, C_S, of 0.037, 0.1, 0.5, and 1.0 wt%. To clean the core between experiments, we used a solution of 50 vol% tap water and 50 vol% isopropyl alcohol. The alcohol purity was 99.7%. We used two cylindrical Bentheimer cores cut from the same outcrop. The length of the cores was 38 cm and their diameter was 3.8 cm. The measured average permeabilities were 2,300 and 2,100 md, respectively. We measured an average porosity of 0.226 for the second core using the CT scanner.

Experimental Procedure

Before each experiment, we injected 10 PV of carbon dioxide (CO_2) to displace any gas inside the core. Next, we injected at least 10 PV of brine at elevated pressure (80 bars) to dissolve any CO_2 that remained in the core. Then we measured the liquid permeability of the core. Finally, we injected 10 PV of surfactant solution to satisfy adsorption.

During each experiment, we performed several foam-quality scans. Foam quality is gas fractional flow [i.e., $(1-f_w)$]. A foam scan is a series of steady-state measurements at different values of f_w and fixed total superficial velocity u_t. Because our goal is to scale up a gas-injection process in SAG, we focus on data at low f_w. In most experiments, we infer water saturation S_w from measured mobility using an estimated water relative-permeability function $k_{rw}(S_w)$ for Bentheimer Sandstone, as discussed later. In one foam scan, we monitored S_w using a medical CT scanner. At the end of each experiment, we cleaned the core as follows, using a procedure similar to that used by Eftekhari and Farajzadeh (2017) and Kahrobaei et al. (2017) on shorter cores. First, we injected 10 PV of a 50/50 water/isopropyl alcohol solution at elevated pressure (80 bar) to kill foam. Second, we injected 10 PV of water initially at elevated (80 bar) backpressure, and we reduced pressure slowly to atmospheric to allow the expansion of trapped gas. Third, we injected 10 PV of CO_2 followed by an additional 10 PV of water at atmospheric pressure. Fourth, we flushed the core again with 20 PV of water while gradually raising the backpressure until its value reached 80 bar. Then we gradually reduced pressure to atmospheric. Fifth, we vacuum-cleaned the core, followed by the injection of at least 10 PV of CO_2. Finally, we performed the preparation procedure described previously and verified that the core had been restored to its initial permeability.

We took ∇P data from the average pressure difference in Sections 2 to 5. We did not use the first or last sections to exclude entrance and capillary end effects in our data. The transducers measure pressure difference across sections 6.7 cm long. The first and last sections may be slightly longer or shorter than 6.7 cm depending on the exact placement of the core in the coreholder, but we use data from the middle four sections below.

In our experiments, we obtained monotonic fractional-flow curves $f_w(S_w)$ in two cases. First, we measured steady-state behavior (illustrated in **Fig. A-1**) when a second front of a much stronger foam did not erupt at the core outlet and subsequently propagate upstream. Second, in cases where such an eruption occurred at the core outlet, we used a foam generator and measured foam mobility in the core behind the foam front before gas breakthrough and eruption of the stronger foam state (illustrated in **Fig. A-2,** which ends just as stronger foam erupts in the last section). In these cases, we verified that foam behind the first foam front was at local equilibrium by comparing pressure data from multiple segments along the core. In agreement with Apaydin and Kovscek (2001), we did not observe this eruption of stronger foam at the outlet in experiments with a relatively low surfactant concentration (0.037 wt%). Further details are in Appendix A.

Foam Model

Foam rheology in porous media can be represented using either implicit-texture or population-balance models. Population-balance models represent foam texture explicitly by dynamic simulation of bubble size (Kam et al. 2007; Kovscek et al. 2010). Gas mobility is then calculated as a function of bubble size. This approach is essential in cases where a foam-generation process is in question or is the object of study. Implicit-texture models represent foam rheology using a mobility-reduction factor (Cheng et al. 2000). Both models represent local equilibrium in a SAG accurately. However, there have been only a few attempts to represent SAG processes with a population-balance model (Kovscek et al. 1995). Therefore, in this study, we chose the STARS™ foam model (Computer Modelling Group 2015), a widely used implicit-texture model (see description in Appendix B). This model predicts relatively strong foam even at irreducible water saturation, S_{wr}. However, a strong foam at irreducible water saturation might not represent long-term foam behavior at the field scale (Rossen et al. 2017; Gong et al. 2019). Therefore, in this study, we also apply the modification of Namdar Zanganeh et al. (2014) that gives complete foam collapse at S_{wr}.

During gas injection in a SAG, our interest is to describe foam behavior at low f_w. Therefore, we focus on the function(s) that describe foam collapse at low f_w: in this case, the dry-out function in the STARS foam model. However, there are cases where the data range includes experimental data at higher f_w (i.e., in both the low-quality and high-quality foam regimes) (Alvarez et al. 2001). To obtain a correct fit at low f_w in these cases, one must include functions that describe non-Newtonian behavior in the low-quality regime. The details about these functions are in Appendix B.

Model Fitting

We start by assuming that a single $k_{rw}(S_w)$ function applies in a given core even in the presence of foam (Huh and Handy 1989; De Vries and Wit 1990; Friedmann et al. 1991; Eftekhari and Farajzadeh 2017). Eftekhari and Farajzadeh (2017) found that the effect of foam on the $k_{rw}(S_w)$ function for relatively high capillary numbers is not pronounced and can be ignored. They obtained a single $k_{rw}(S_w)$ fit for a set of data with measurements of pressure gradient and water saturation in the absence and presence of foam. We describe the parameters of this $k_{rw}(S_w)$ function in detail in Appendix B. They used a Bentheimer core with a permeability of 2,410 md, which is similar to that measured in our own experiments. They used two different surfactants and varied the value of C_S for one of these surfactants (AOS). They varied C_S of the AOS surfactant in a similar manner as we do in this study. The value of S_w inferred from ∇P data are then the value that satisfies Darcy's law for the water phase in foam:

$$u_t f_w = -\frac{k\ k_{rw}(S_w)}{\mu_w}\nabla P. \qquad (1)$$

We test if this function correctly estimates S_w data measured with the CT scanner in our own experiments. To that end, we performed a foam scan while measuring water saturation using a CT scanner. We performed this foam scan at a total superficial velocity of 4.25 ft/D (1.47×10^{-5} m/s) with $C_S = 0.5$ wt%. The black circles in **Fig. 4** illustrate the fractional-flow data as function of water saturation $f_w(S_w)$ in two sections of the core at steady state. In this case, we report the measured water saturation with the CT scanner. The gray squares in Fig. 4 illustrate $f_w(S_w)$ data for the same foam scan, inferring water saturation using the $k_{rw}(S_w)$ function for a Bentheimer core reported by Eftekhari and Farajzadeh (2017). The black triangles in Fig. 4 report $f_w(S_w)$ data where S_w was inferred using the $k_{rw}(S_w)$ function reported by Kapetas et al. (2017), which was measured only in the absence of foam. Both k_{rw} functions correctly predict within experimental error the trend in which S_w increases with decreasing f_w seen in the CT data. We discuss the implications of the nonmonotonic trend in $f_w(S_w)$ in Salazar and Rossen (2019). From our own data, it is clear that the $k_{rw}(S_w)$ function reported by Eftekhari and Farajzadeh (2017) better reflects the water saturations measured with the CT scanner in our own experiments. Moreover, because the function was measured by Eftekhari and Farajzadeh (2017) over a wide range of surfactant concentrations C_S, we assume it is suitable for analyzing our foam scans performed at different values of C_S. For the sake of simplicity, in this study, we analyze our experimental data using a single $k_{rw}(S_w)$ function: the one that is fitted over a wide range of surfactant concentrations. Nevertheless, for our sensitivity analysis, as we explain later, we use the $k_{rw}(S_w)$ function reported by Kapetas et al. (2017) to illustrate the sensitivity of scaled-up mobility and injectivity to the choice of $k_{rw}(S_w)$ function. We include the parameters of this function also in Appendix B.

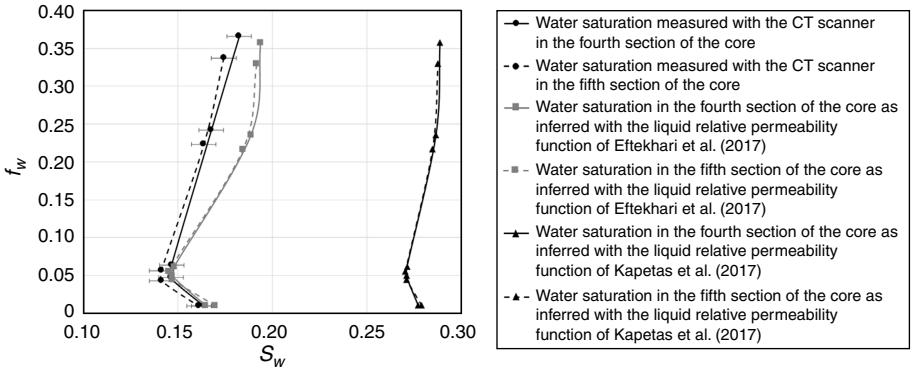

Fig. 4—Fractional-flow curves $f_w(S_w)$ for a foam scan performed at a total superficial velocity of 4.21 ft/D (1.48×10^{-5} m/s) with $C_S = 0.5$ wt%. Black circles, S_w was measured directly using a CT scanner; gray squares, S_w is inferred using the $k_{rw}(S_w)$ function presented by Eftekhari and Farajzadeh (2017); black triangles, S_w is inferred using the $k_{rw}(S_w)$ function reported by Kapetas et al. (2017) with no foam present. We calculated a standard deviation in the CT-measured S_w values of 0.006 (illustrated by error bars) and a standard deviation in the value of S_w estimated from ∇P data (based on the variation of ∇P along the core) of 0.001 (error bars not visible at the figure scale).

We fit the $f_w(S_w)$ data using two methods. The first method (Eftekhari and Farajzadeh 2017; Kapetas et al. 2017) is a least-squares optimization routine that fits the model parameters to apparent viscosity over a wide scan of foam qualities. This method assigns equal weight to all the experimental points in a foam scan, including those in the low-quality regime. The second method focuses on experimental data in the high-quality regime (Rossen and Boeije 2015), specifically near the point of tangency (cf. Fig. 1). This method involves visual comparison of the data and the model fit. Therefore, the obtained parameters might not be unique. We illustrate the sensitivity to how this fit is done by making three different fits to the mobility data of one of the foam scans using three different criteria. We describe the parameters used in both methods in Appendix B. With the model parameters obtained, we scale up to a hypothetical field application, as in Appendix C. The parameter corresponding to the water saturation at which foam abruptly weakens, S_w*, or *fmdry* in the STARS foam model, is fixed in all our fits in which we used the method of Rossen and Boeije (2015). We fit the $f_w(S_w)$ data using a least-squares fit to the entire foam scan (Eftekhari and Farajzadeh 2017; Kapetas et al. 2017), using a first guess based on the method of Boeije and Rossen (2015a). Therefore, for each foam scan, we obtain four parameter sets, where two were obtained with the method of Rossen and Boeije (2015) for a SAG and two using the fit to the entire foam scan. Finally, we perform the fits again using the model correction of Namdar Zanganeh et al. (2014), here denoted as NZ. This modification gives complete foam collapse at S_{wr}, which is expected if foam stability depends on capillary pressure (Khatib et al. 1988). We show the sensitivity of the scaled-up injectivity and mobility control at the shock at the field scale to the method of fitting the parameters and in the presence and absence of the correction of NZ.

Sometimes a suitable $k_{rw}(S_w)$ function is not available in the literature for a particular core sample. Therefore, we illustrate the sensitivity of predicted field performance to the liquid relative-permeability function, $k_{rw}(S_w)$, and the gas relative-permeability function, $k_{rg}(S_w)$, by again doing the model fit using the functions reported by Kapetas et al. (2017). Then, we compare the mobility at the shock and injectivity predicted by these new parameter sets against our previous results.

Results

As mentioned above, for a relatively low C_S (0.037 wt%), there was no eruption of stronger foam at the core outlet, and we use steady-state data; an example can be found in Appendix A. For greater concentrations (0.1, 0.5, and 1.0 wt%), we used a foam generator. In these cases, where a stronger foam erupts at the core outlet at foam breakthrough, we report local-equilibrium mobility in the foam bank before foam breakthrough (i.e., before 1 PV, as can be seen in Appendix A).

In all the experiments reported here, we found consistently uniform pressure gradients in the intermediate sections of the core (excluding the entrance and exit regions), despite increasing gas superficial velocity downstream caused by modest effects of gas expansion. This is expected for foam in the high-quality regime (Alvarez et al. 2001).

Fig. 5 shows the experimental data corresponding to the five foam scans performed in this study. This figure shows apparent foam viscosity, μ_{app}, as function of foam quality, $f_g = (1 - f_w)$. We define apparent viscosity as $\mu_{app} = [k\nabla P/(Lu_t)]$, where k and L denote rock permeability and the length of the core section used, and ∇P is the pressure difference across that section, respectively. Fig. 5 also shows the model fit to the whole foam scan using the least-squares approach used by Eftekhari and Farajzadeh (2017) and Kapetas et al. (2017).

Fig. 6 illustrates the experimental data around the point of tangency for each of the five foam scans performed in this study. We plot the $f_w(S_w)$ data using the symbols of the corresponding foam scan in Fig. 5. In all of these plots, we inferred S_w using the foam-scan data in combination with the $k_{rw}(S_w)$ function reported by Eftekhari and Farajzadeh (2017); see Appendix B for a complete description of the $k_{rw}(S_w)$ functions used in this study. On the left of Fig. 6, we plot the $f_w(S_w)$ curves corresponding to the parameters obtained with the least-squares optimization of the whole foam scan. On the right, we plot the $f_w(S_w)$ curves corresponding to the parameters obtained using the method of Rossen and Boeije (2015) for a SAG. The complete set of parameters obtained with the least-squares optimization and the method of Rossen and Boeije (2015) are summarized in **Tables 1** and **2,** respectively. We provide a complete description of the foam parameters used in this study in Appendix A. The shocks for a gas-injection process are represented in Fig. 6 by solid black lines. The mobilities just behind these shocks in $(\text{Pa}\cdot\text{s})^{-1}$ predicted by the corresponding model fit are listed in Tables 1 and 2. We calculate these mobilities using the equation $\lambda_{rt} = k_{rw}(S_w)/(f_w\ \mu_w)$, where μ_w denotes the water viscosity, here equal to 1.0 (mPa·s). This viscosity corresponds to a mobility of $\lambda_w = 1.0\times10^3$ $(\text{Pa}\cdot\text{s})^{-1}$. Every set of data predicts excellent mobility control at the leading edge of the foam bank.

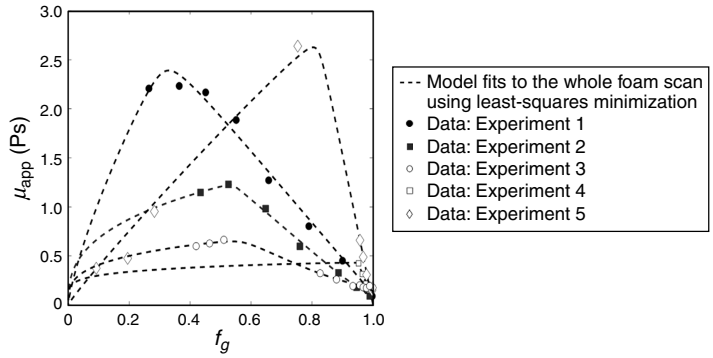

Fig. 5—Experimental data for the five foam scans performed in this study. Experiment 1 denotes the foam scan performed with $u_t = 2.94\times10^{-6}$ m/s and $C_S = 0.037$ wt%. Experiment 2 is the data for $u_t = 7.35\times10^{-6}$ m/s and $C_S = 0.037$ wt%. Experiment 3 is the data with $u_t = 1.47\times10^{-5}$ m/s and $C_S = 0.1$ wt%. Experiment 4 is the data with $u_t = 1.47\times10^{-5}$ m/s and $C_S = 0.5$ wt%. Experiment 5 is with $u_t = 7.35\times10^{-6}$ m/s and $C_S = 1.0$ wt% AOS. The dashed lines denote the model fit to the whole foam scan in each case using least-squares minimization.

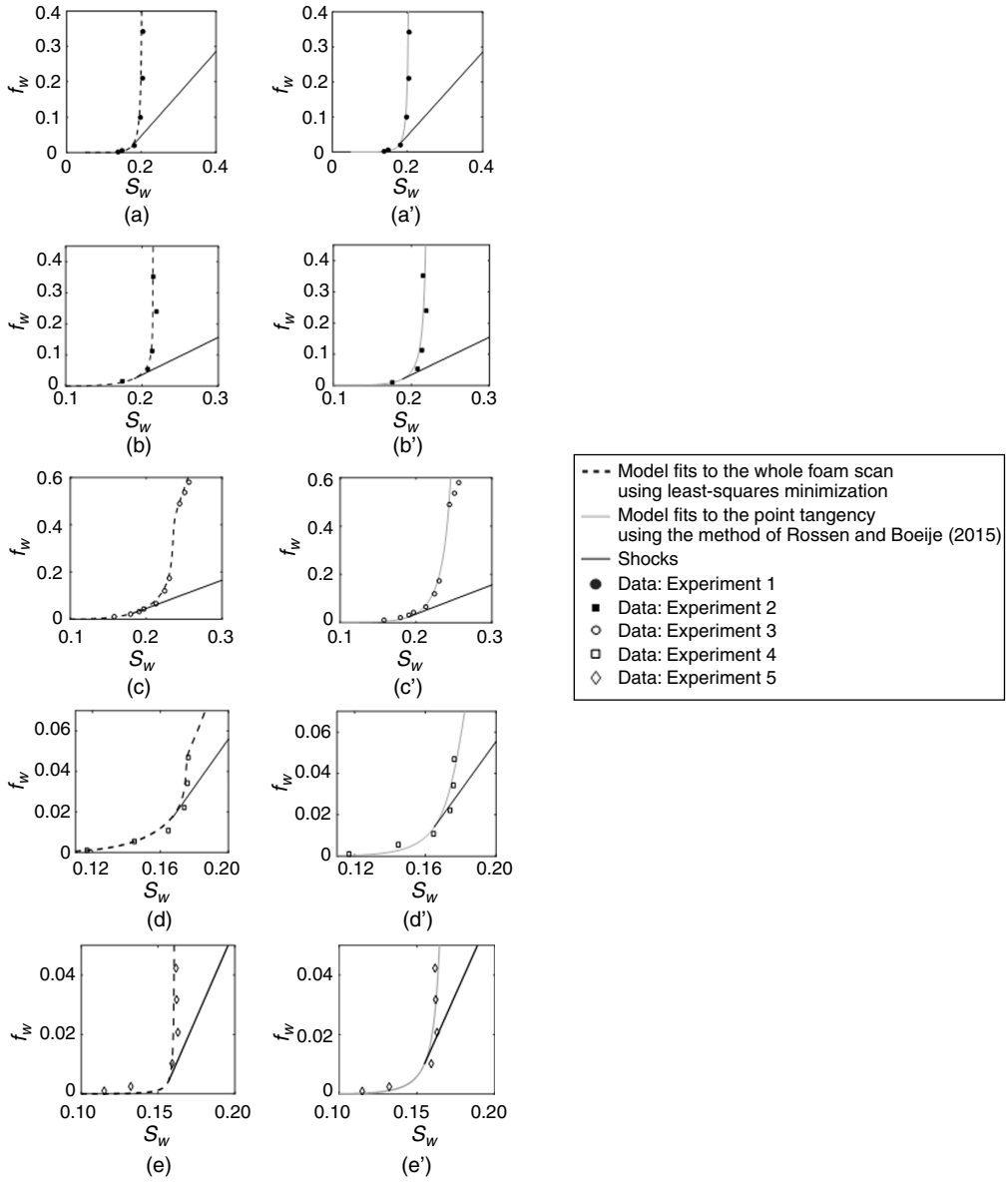

Fig. 6—Experimental data around the point of tangency corresponding to the foam scans presented in Fig. 5. (Left) $f_w(S_w)$ curves predicted by the model fit performed using the whole foam scan. (Right) $f_w(S_w)$ curves obtained using the method of Rossen and Boeije (2015) for a SAG (middle estimate; see the sensitivity analysis in the Results section). Solid lines correspond to the predicted shocks during a gas-injection process.

Foam Parameters Optimized to the Entire Foam Scan

	Experiment 1	Experiment 2	Experiment 3	Experiment 4	Experiment 5
C_S (wt%)	0.037	0.037	0.1	0.5	1.0
u_t (m/s)	2.94×10^{-6}	7.35×10^{-6}	1.47×10^{-5}	1.47×10^{-5}	7.35×10^{-6}
u_t (ft/D)	0.83	2.12	4.25	4.25	2.12
STARS					
$k_{rw}(S_w)$ Function	Eftekhari and Farajzadeh (2017)				
fmdry	0.202	0.214	0.234	0.175	0.161
fmmob	2.98×10^{5}	9.33×10^{5}	9.47×10^{8}	5.47×10^{6}	8.71×10^{4}
epdry	812	2,294	1,766	1,654	3,446
fmcap	5.00×10^{-6}	2.00×10^{-5}	1.00×10^{-5}	5.00×10^{-5}	1.0×10^{-5}
epcap	0.09	1.00	3.00	4.26	0
$fmmob_{SAG}$	2.67×10^{5}	5.93×10^{5}	1.23×10^{6}	2.23×10^{5}	8.71×10^{4}
max P_D	44.1	32.8	63.0	30.8	13.1
λ_{rt} $(Pa\cdot s)^{-1}$	6.6	8.7	6.0	7.2	13.0
NZ Correction					
$k_{rw}(S_w)$ Function	Eftekhari and Farajzadeh (2017)				
fmdry-NZ	0.202	0.214	0.234	0.175	0.161
fmmob-NZ	2.98×10^{5}	9.33×10^{5}	9.47×10^{8}	5.47×10^{6}	8.71×10^{4}
epdry-NZ	812	2,294	1,766	1,654	3,249
fmcap-NZ	5.00×10^{-6}	2.00×10^{-5}	1.00×10^{-5}	5.00×10^{-5}	1.0×10^{-5}
epcap-NZ	0.09	1.00	3.00	4.26	0
$fmmob_{SAG}$-NZ	2.67×10^{5}	5.93×10^{5}	1.23×10^{6}	2.23×10^{5}	8.71×10^{4}
max P_D NZ	22.9	17.3	25.3	20.3	10.9
λ_{rt} $(Pa\cdot s)^{-1}$ NZ	7.6	10.0	7.6	7.8	13.5

We include the predicted total relative mobility, λ_{rt}, behind the shock front in $(Pa\cdot s)^{-1}$ and the maximum dimensionless pressure, P_D, reached during gas injection.

Table 1—Foam parameters obtained by the least-squares routine used by Eftekhari and Farajzadeh (2017) and Kapetas et al. (2017).

Foam Parameters Optimized to the Point of Tangency

	Experiment 1	Experiment 2	Experiment 3	Experiment 4	Experiment 5
C_S (wt%)	0.037	0.037	0.1	0.5	1.0
u_t (m/s)	2.94×10^{-6}	7.35×10^{-6}	1.47×10^{-5}	1.47×10^{-5}	7.35×10^{-6}
u_t (ft/D)	0.83	2.12	4.25	4.25	2.12
STARS					
$k_{rw}(S_w)$ Function	Eftekhari and Farajzadeh (2017)				
fmdry	0.204	0.22	0.25	0.18	0.167
fmmob	5.00×10^{5}	5.00×10^{5}	4.00×10^{5}	2.5×10^{4}	6.50×10^{4}
epdry	1,300	1,600	600	75	300
max P_D	49.0	36.1	54.5	55.5	47.9
λ_{rt} $(Pa\cdot s)^{-1}$	6.2	8.4	7.2	4.8	4.9
NZ Correction					
$k_{rw}(S_w)$ Function	Eftekhari and Farajzadeh (2017)				
fmdry-NZ	0.204	0.22	0.25	0.18	0.167
fmmob-NZ	5.00×10^{5}	4.00×10^{5}	4.00×10^{5}	2.5×10^{4}	6.50×10^{4}
epdry-NZ	1,000	1,100	480	50	220
max P_D	28.6	19.7	24.3	38.0	35.7
λ_{rt} $(Pa\cdot s)^{-1}$	6.3	9.1	8.2	4.6	4.6

In the last row we include the predicted total relative mobility, λ_{rt}, behind the shock front during gas injection in $(Pa\cdot s)^{-1}$.

Table 2—Foam parameters derived using the method of Rossen and Boeije (2015) for SAG.

We calculate the inverse of injectivity using a dimensionless pressure, P_D, which measures how the scaled-up pressure at the injection well compares with that expected when injecting water into the same reservoir at the same volumetric rate. For instance, this means that a $P_D = 5$ for foam injection corresponds to five times the rise in pressure at the wellbore when injecting water into the reservoir at the same volumetric injection rate. For this scaleup, we assume a cylindrical and homogenous reservoir; we explain our approach in detail in Appendix C. For the strong foams reported here, the dimensionless pressure rises abruptly at the very beginning of gas injection and stays nearly constant until foam breaks through, as illustrated in **Fig. C-1** (cf. Boeije and Rossen 2015b). Therefore, we report in Tables 1 and 2 the maximum dimensionless pressure (here denoted as max P_D,) during a gas-injection process.

In this study, we focus on capturing correctly the point of tangency for all our experiments. Although the model fits use different methodologies and obtain different sets of parameters, both give nearly the same mobility at the shock and injectivity for Experiments 1, 2, and 3, as we summarize in Tables 1 and 2. However, we found that the least-squares model fit to the whole foam scan for Experiments 4 and 5 fails to capture the trend followed by the experimental points near the point of tangency. For example, in Fig. 6e, the model fit deviates from the trend of the data below $f_w = 0.005$. This failure produces an underestimation of the mobility control behind the shock front: the least-squares fit to the whole quality scan predicts a mobility of 15.25 $(\text{Pa}\cdot\text{s})^{-1}$ behind the shock, whereas the method of Rossen and Boeije (2015), based on the closer fit to data in this range, provides an estimate of 5.36 $(\text{Pa}\cdot\text{s})^{-1}$. In this case, the method of Rossen and Boeije (2015) for a SAG gives a better estimate of the mobility behind the shock. However, the method of Rossen and Boeije (2015) does not always have a good fit at lower foam qualities (greater f_w), as is evident at the top part of Fig. 6c.

We next test the sensitivity of the resulting foam parameters to the modification of Namdar Zanganeh et al. (2014) (NZ). For the model fit to the whole foam scan, the NZ modification does not affect the parameters obtained, as we summarize in Table 1. For the model fit using the method of Rossen and Boeije (2015) for a SAG, the parameters *fmmob* and/or *epdry* do differ when using the NZ correction, as we present in Table 2. Ideally, this variation is not expected because the correction was designed to affect foam mobility specifically near S_{wr}. The resulting total relative mobilities, λ_{rt}, at the shock front are practically the same, as we present in Table 2 and illustrate in **Fig. 7.** In addition, the consistent reduction of the maximum dimensionless pressure, max P_D, in the presence of the NZ correction, as depicted in Tables 1 and 2, illustrates the improvement in injectivity if foam collapses completely at S_{wr}.

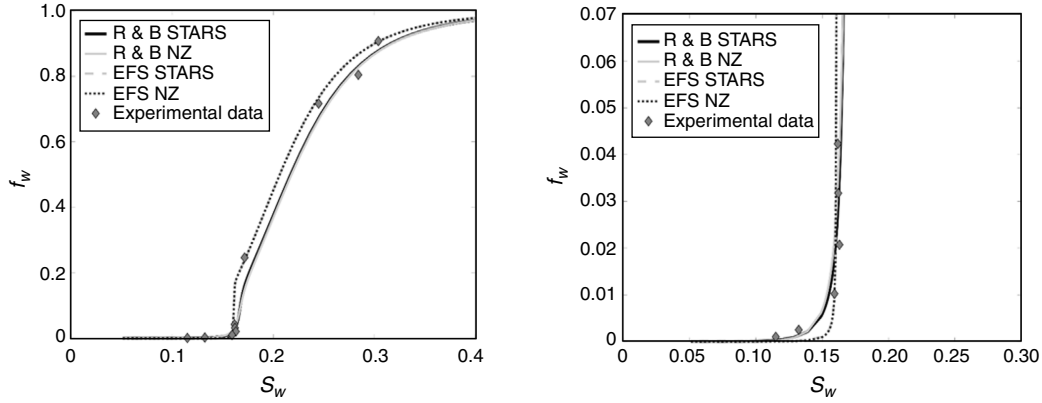

Fig. 7—Four model fits for the data of Experiment 5. We performed two model fits using the method of Rossen and Boeije (2015) for a SAG: one without the NZ correction (here labeled as R&B STARS) and one with the NZ correction (here labeled as R&B NZ). We performed the other two model fits using the method of Eftekhari et al. (2017) to the entire foam scan: with and without the NZ correction, here labeled EFS STARS and EFS NZ, respectively. On the right, we present an expanded view near the tangency point.

We also test the variability in the resulting parameters when using the method of Rossen and Boeije (2015) for a SAG, which relies on visual inspection. To that end, we perform a second fit and a third fit for the data of Experiment 4. In our first fit, presented in Table 2, we imagine a criterion (Criterion 1) that focuses on obtaining a best middle estimate for all the experimental data. In the second fit, we imagine Criterion 2 that focuses on fitting data at relatively high f_w but accepts a poor fit around the point of tangency at $f_w = 0.01$ and 0.005. Finally, Criterion 3 focuses on fitting the tangency condition as closely as possible, but disregards data at f_w well above the point of tangency. We present the resulting fits in **Fig. 8,** and we summarize the foam parameters and the upscaled values in **Table 3.** On one hand, Criterion 2 does not capture the point of tangency well, and the scaling up underestimates mobility control at the leading edge of the foam bank. Criteria 1 and 3 have similar estimates for mobility control at the leading edge and injectivity.

In the absence of liquid-saturation data, we could have used a different $k_{rw}(S_w)$ function available in the literature. Therefore, we also test the role of the choice of a particular $k_{rw}(S_w)$ function on the predicted λ_{rt} behind the shock and in the injectivity during gas injection. This is important because sometimes the $k_{rw}(S_w)$ function has not been measured for a particular porous medium. We start our analysis considering the $k_{rw}(S_w)$ parameters published by Kapetas et al. (2017); we present a complete description of this function in Appendix B. This function was not able to reproduce the water-saturation measurements from our CT scans, as illustrated in Fig. 4. Nevertheless, for illustration purposes, we use the function to calculate the corresponding water saturations for each experimental point. Thereafter, we carry out the model fit using the method of Rossen and Boeije (2015). **Fig. 9** illustrates the model fit, and **Table 4** summarizes the parameters obtained, together with max P_D and λ_{rt}. The mobility behind the shock increases to 7.31 $(\text{Pa}\cdot\text{s})^{-1}$, whereas the calculated injectivity remains practically the same. Although the water saturations are very different (Fig. 4), this function can be used to obtain a reasonable estimate for injectivity, and the mobility at the shock is not very different from that with the other $k_{rw}(S_w)$ function. This could be explained by the fact that we use the same pressure data from the foam scan of Experiment 4 to infer both curves. This could, of course, fail if the $k_{rw}(S_w)$ function completely failed to represent true behavior.

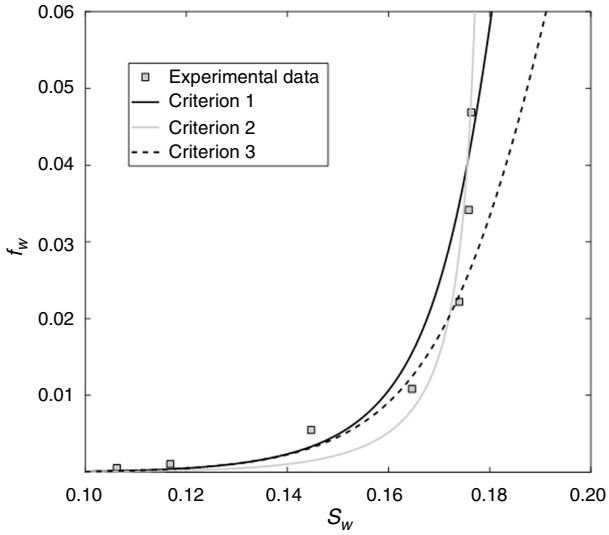

Fig. 8—Model fits from the sensitivity test of the method of Rossen and Boeije (2015). In the test, we use three different criteria. The experimental data are from Experiment 4. The corresponding foam parameters are listed in Table 3.

	Experiment 4		
Fitting Criteria	Criterion 1	Criterion 2	Criterion 3
	STARS		
$k_{rw}(S_w)$ Function	Eftekhari and Farajzadeh (2017)		
fmdry	0.18	0.18	0.18
fmmob	2.5×10^4	1×10^5	1.4×10^4
epdry	75	700	40
max P_D	55.5	29.9	56.2
λ_{rt} (Pa·s)$^{-1}$	4.8	7.6	4.9

We include the maximum dimensionless pressure, max P_D, and the total relative mobility, λ_{rt}, behind the shock front during gas injection in (Pa·s)$^{-1}$. See description in the text.

Table 3—Foam parameters resulting from the sensitivity test for the method of Rossen and Boeije (2015).

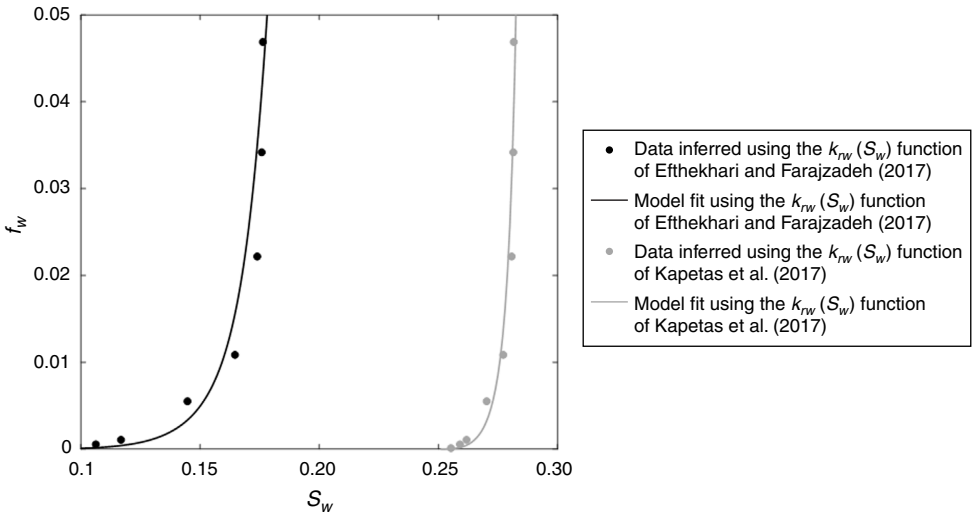

Fig. 9—Two fits using different $k_{rw}(S_w)$ functions for the data of Experiment 4 using the method of Rossen and Boeije (2015). We summarize the resulting foam parameters in Table 4.

	Experiment 4	
Fitting Criteria	Criterion 1	Criterion 1
	STARS	
$k_{rw}(S_w)$ function	Eftekhari and Farajzadeh (2017)	Kapetas et al. (2017)
fmdry	0.18	0.285
fmmob	2.5×10^4	4×10^4
epdry	75	280
max P_D	55.5	55.5
λ_{rt} (Pa·s)$^{-1}$	4.8	7.3

We use two different $k_{rw}(S_w)$ functions. We include the maximum dimensionless pressure, max P_D, and the total relative mobility, λ_{rt}, behind the shock front during gas injection in (Pa·s)$^{-1}$.

Table 4—Foam parameters fit using the method of Rossen and Boeije (2015).

Discussion and Conclusions

For gas injection in a SAG application, the most suitable fitting method is the method of Rossen and Boeije (2015). The method can estimate the tangency conditions in all of our experiments. The method of Eftekhari and Farajzadeh (2017) to the entire foam scan may produce a poor estimation of mobility control at the shock. However, the method of Rossen and Boeije can give a poorer fit at higher values of f_w that apply where gas and liquid slugs mix away from the well.

The method of Rossen and Boeije (2015) might seem limited by relying on visual inspection and by the criteria used in performing the fit. However, for the cases examined here, the impact of these factors is modest given the uncertainty in other factors. For instance, in the worst-case scenario of our sensitivity analysis, the difference between our best and worst estimates for mobility control is 2.8 (Pa·s)$^{-1}$ (an approximate 50% difference in mobility), which is not significantly larger than the difference of 2.5 (Pa·s)$^{-1}$ arising from selection of an inaccurate liquid relative-permeability function.

We also find that injectivity can be estimated reasonably well using a different liquid relative-permeability function. This could, of course, fail if the $k_{rw}(S_w)$ function completely fails to represent true behavior.

If foam collapses at S_{wr}, the NZ correction is key in better reproducing the injectivity observed at the field scale. For the fits presented here, the correction slightly affects the fit to data in the range measured. Therefore, the optimized foam parameters change slightly. The predicted mobility control at the leading edge of the foam bank with and without the correction are nearly the same.

In all our experiments, neither of the two methods is able to capture the trends of the experimental points in both the low-quality and high-quality regimes using the same set of parameters or fit. We suggest keeping this compromise in mind when performing a model fit using any of the methods discussed here.

Our limited data suggest that increasing the surfactant concentration improves mobility control. Also, it suggests that the effect of total superficial velocity is limited. In other words, for the two velocities studied here, at the same surfactant concentration, the corresponding foams behave in good agreement with a Newtonian rheology in the high-quality regime.

References

Al Ayesh, A. H., Salazar, R., Farajzadeh, R. et al. 2017 Foam Diversion in Heterogeneous Reservoirs: Effect of Permeability and Injection Method. *SPE J.* **22** (5): 1402–1415. SPE-179650-PA. https://doi.org/10.2118/179650-PA.

Alvarez, J. M., Rivas, H., and Rossen, W. R. 2001. A Unified Model for Steady-State Foam Behavior at High and Low Foam Qualities. *SPE J.* **6** (3): 325–333. SPE-74141-PA. https://doi.org/10.2118/74141-PA.

Apaydin, O. G. and Kovscek, A. R. 2001. Surfactant Concentration and End Effects on Foam Flow in Porous Media. *Transport Porous Media* **43** (3): 511–536. https://doi.org/10.1023/A:1010740811277.

Boeije, C. S. and Rossen, W. R. 2015a. Fitting Foam-Simulation-Model Parameters to Data: I. Co-Injection of Gas and Liquid. *SPE Res Eval & Eng* **18** (2): 264–272. SPE-174544-PA. https://doi.org/10.2118/174544-PA.

Boeije, C. S. and Rossen, W. R. 2015b. Gas Injection Rate Needed for SAG Foam Processes To Overcome Gravity Override. *SPE J.* **20** (1): 49–59. SPE-166244-PA. https://doi.org/10.2118/166244-PA.

Boeije, C. S. and Rossen, W. R. 2018. SAG Foam Flooding in Carbonate Rocks. *J Pet Sci & Eng* **171:** 843–853. https://doi.org/10.1016/j.petrol.2018.08.017.

Cheng, L., Reme, A. B., Shan, D. et al. 2000. Simulating Foam Processes at High and Low Foam Qualities. Paper presented at the SPE/DOE Improved Oil Recovery Symposium, Tulsa, Oklahoma, USA, 3–5 April. SPE-59287-MS. https://doi.org/10.2118/59287-MS.

Computer Modelling Group Ltd. 2015. *CMG-STARS User's Guide*, Calgary, Alberta, Canada: Computer Modelling Group Ltd.

De Velde Harsenhorst, R. M., Dharma, A. S., Andrianov A. et al. 2014. Extension and Verification of a Simple Model for Vertical Sweep in Foam Surfactant-Alternating-Gas Displacements. *SPE Res Eval & Eng* **17** (3): 373–383. SPE-164891-PA. https://doi/org/10.2118/164891-PA.

De Vries, A. S. and Wit, K. 1990. Rheology of Gas/Water Foam in the Quality Range Relevant to Steam Foam. *SPE Res Eng* **5** (2): 185–192. SPE-18075-PA. https://doi.org/10.2118/18075-PA.

Eftekhari, A. A. and Farajzadeh, R. 2017. Effect of Foam on Liquid Phase Mobility in Porous Media. *Sci Rep* **7:** 43870. https://doi.org/10.1038/srep43870.

Farajzadeh, R., Lotfollahi, M., Eftekhari, A. A. et al. 2015. Effect of Permeability on Implicit-Texture Foam Model Parameters and the Limiting Capillary Pressure. *Energy & Fuels* **29** (5): 3011–3018. https://doi.org/10.1021/acs.energyfuels.5b00248.

Friedmann, F., Chen, W. H., and Gauglitz, P. A. 1991. Experimental and Simulation Study of High-Temperature Foam Displacement in Porous Media. *SPE Res Eng* **6** (1): 37–45. SPE-17357-PA. https://doi.org/10.2118/17357-PA.

Gong, J., Vincent-Bonnieu, S., Kamarul Bahrim, R. Z. et al. 2019. Modelling of Liquid Injectivity in Surfactant-Alternating-Gas Foam Enhanced Oil Recovery. *SPE J.* **24** (3): 1123–1138. SPE-190435-PA. https://doi.org/10.2118/190435-PA.

Heller, J. P. 1994. CO_2 Foams in Enhanced Oil Recovery in Foams: Fundamentals and Applications in the Petroleum Industry. In *Advances in Chemistry*, ed L. L. Schramm, 201–234. Washington, DC, USA: American Chemical Society. https://doi.org/10.1021/ba-1994-0242.fw001.

Huh, D. G. and Handy, L. L. 1989. Comparison of Steady and Unsteady-State Flow of Gas and Foaming Solution in Porous Media. *SPE Res Eng* **4** (1): 77–84. SPE-15078-PA. https://doi.org/10.2118/15078-PA.

Jacobsen, R. T. and Stewart, R. B. 1973. Thermodynamic Properties of Nitrogen Including Liquid and Vapor Phases from 63K to 2000K with Pressures to 10,000 Bar. *Journal of Physical and Chemical Reference Data* **2** (4): 757–922. https://doi.org/10.1063/1.3253132.

Kahrobaei, S., Vincent-Bonnieu, S., and Farajzadeh, R. 2017. Experimental Study of Hysteresis Behavior of Foam Generation in Porous Media. *Sci Rep* **7:** 8986. https://doi.org/10.1038/s41598-017-09589-0.

Kam, S. I., Nguyen, Q. P., and Rossen, W. R. 2007. Dynamic Simulations with and Improved Model for Foam Generation. *SPE J.* **12** (1): 35–48. SPE-90938-PA. https://doi.org/10.2118/90938-PA.

Kapetas, L., van El, W. A., and Rossen, W. R. 2014. Representing Slow Foam Dynamics in Laboratory Corefloods for Enhanced Oil Recovery. Paper presented at the SPE Improved Oil Recovery Symposium, Tulsa, Oklahoma, USA, 12–16 April. SPE-169059-MS. https://doi.org/10.2118/169059-MS.

Kapetas, L., Vincent-Bonnieu, S., Farajzadeh, R. et al. 2017. Effect of Permeability on Foam-Model Parameters: An Integrated Approach from Core-Flood Experiments through to Foam Diversion Calculations. *Colloids & Surf A: Physicochem & Eng Aspects* **530:** 172–180. https://doi.org/10.1016/j.colsurfa.2017.06.060.

Khatib, Z. I., Hirasaki, G. J., and Falls, A. H. 1988. Effects of Capillary Pressure on Coalescence and Phase Mobilities in Foams Flowing Through Porous Media. *SPE Res Eng* **3** (3): 919–926. SPE-15442-PA. https://doi.org/10.2118/15442-PA.

Kibodeaux, K. R. and Rossen, W. R. 1997. Coreflood Study of Surfactant-Alternating-Gas Foam Processes: Implications for Field Design. Paper presented at the SPE Western Regional Meeting, Long Beach, California, USA, 25–27 June. SPE-38318-MS. https://doi.org/10.2118/38318-MS.

Kloet, M. B., Renkema, W. J., and Rossen, W. R. 2009. Optimal Design Criteria for SAG Foam Processes in Heterogeneous Reservoirs. Paper presented at the SPE Europec/EAGE Annual Conference and Exhibition, Amsterdam, The Netherlands, 8–11 June. SPE-121581-MS. https://doi.org/10.2118/121581-MS.

Kovscek, A. R., Chen, Q., and Gerritsen, M. 2010. Modelling Foam Displacement with the Local-Equilibrium Approximation: Theory and Experimental Verification. *SPE J.* **15** (1): 171–183. SPE-116735-PA. https://doi.org/10.2118/116735-PA.

Kovscek, A. R., Patzek, T. W., and Radke, C. J. 1995. A Mechanistic Population Balance Model for Transient and Steady-State Foam Flow in Boise Sandstone. *Chem Eng Sci* **50** (23): 3798–3799. https://doi.org/10.1016/0009-2509(95)00199-F.

Lake, L. W., Johns, R. T., Rossen, W. R. et al. 2014. *Fundamentals of Enhanced Oil Recovery*. Richardson, Texas, USA: Society of Petroleum Engineers.

Matthews, C. S. 1989. Carbon Dioxide Flooding. *Dev Pet Sci* **17:** 129–156. https://doi.org/10.1016/S0376-7361(08)70458-8.

Namdar Zanganeh, M., Kraaijevanger, J. F. B. M., Buurman, H. W. et al. 2014. Challenges to Adjoint-Based Optimization of a Foam EOR Process. *Comput Geosci* **18** (3–4): 563–577. https://doi.org/10.1007/s10596-014-9412-4.

Nguyen, Q. P., Currie, P. K., and Zitha, P. L. J. 2003. Determination of Foam Induced Fluid Partitioning in Porous Media Using X-Ray Computed Tomography. Paper presented at the International Symposium on Oilfield Chemistry, Houston, Texas, USA, 5–7 February. SPE-80245-MS. https://doi.org/10.2118/80245-MS.

Nguyen, Q. P., Rossen, W. R., Zitha, P. L. J. et al. 2009. Determination of Gas Trapping with Foam Using X-Ray Computed Tomography and Effluent Analysis. *SPE J.* **14** (2): 222–236. SPE-94764-PA. https://doi.org/10.2118/94764-PA.

Osterloh, W. T. and Jante, M. J. 1992. Effects of Gas and Liquid Velocity on Steady-State Foam Flow at High Temperature. Paper presented at the SPE/DOE Enhanced Oil Recovery Symposium, Tulsa, Oklahoma, USA, 22–24 April. SPE-24179-MS. https://doi.org/10.2118/24179-MS.

Ransohoff, T. C. and Radke, C. J. 1988. Mechanism of Foam Generation on Glass-Bead Packs. *SPE Res Eval & Eng* **3** (2): 573–585. SPE-15441-PA. https://doi.org/10.2118/15441-PA.

Rossen, W. R. 1996. Foams in Enhanced Oil Recovery. In *Foams: Theory, Measurements and Applications*, eds. R. K. Prud'homme and S. Khan. New York, New York, USA: Marcel Dekker.

Rossen, W. R. and Boeije, C. S. 2015. Fitting Foam-Simulation-Model Parameters to Data: II. Surfactant-Alternating-Gas Foam Applications. *SPE Res Eval & Eng* **18** (2): 273–283. SPE-165282-PA. https://doi.org/10.2118/165282-PA.

Rossen, W. R. and Bruining, J. 2007. Foam Displacements with Multiple Steady States. *SPE J.* **12** (1): 5–18. SPE-89397-PA. https://doi.org/10.2118/89397-PA.

Rossen, W. R., Ocampo, A. A., Restrepo, A. et al. 2017. Long-Time Diversion in Surfactant-Alternating-Gas Foam Enhanced Oil Recovery from a Field Test. *SPE Res Eval & Eng* **20** (1): 1–7. SPE-170809-PA. https://doi.org/10.2118/170809-PA.

Salazar, R. and Rossen, W. 2019. Coreflood Study of NonMonotonic Fractional-Flow Behavior with Foam: Implications for Surfactant-Alternating-Gas Foam EOR. Paper presented at the EAGE IOR Symposium, Pau, France, 8–10 April. http://doi.org/10.3997/2214-4609.201900109.

Salazar Castillo, R. O. 2019. *Scale-Up of Surfactant Alternating Gas Foam Processes*. PhD dissertation, Delft University of Technology, Delft, The Netherlands.

Salazar Castillo, R. O., Ter Haar, S. F., Ponners, C. G. et al. 2020. Fractional-Flow Theory for Non-Newtonian Surfactant-Alternating-Gas Foam Processes. *Transp Porous Med* **131:** 399–426. https://doi.org/10.1007/s11242-019-01351-6.

Schramm, L. L. 1994. *Foams: Fundamentals and Applications in the Petroleum Industry*. Washington, DC, USA: American Chemical Society. https://doi.org/10.1021/ba-1994-0242.

Shan, D. and Rossen, W. R. 2004. Optimal Injection Strategies for Foam IOR. *SPE J.* **9** (2): 132–150. SPE-88811-PA. https://doi.org/10.2118/88811-PA.

Simjoo, M., Dong, Y., Andrianov, A. et al. 2013. CT Scan Study of Immiscible Foam Flow in Porous Media for Enhancing Oil Recovery. *Indust & Eng Chem Res* **52** (18): 6221–6233. https://doi.org/10.1021/ie300603v.

Wassmuth, R. F., Green, K. A., and Randall, L. 2001. Details of In-Situ Foam Propagation Exposed with Magnetic Resonance Imaging. *SPE Res Eval & Eng* **4** (2): 135–145. SPE-71300-PA. https://doi.org/10.2118/71300-PA.

Xu, Q. and Rossen, W. R. 2004. Experimental Study of Gas Injection in Surfactant-Alternating-Gas Foam Process. *SPE Res Eval & Eng.* **7** (6): 438–448. SPE-84183-PA. https://doi.org/10.2118/84183-PA.

Zhou, Z. H. and Rossen, W. R. 1995. Applying Fractional-Flow Theory to Foam Processes at the 'Limiting Capillary Pressure.' *SPE Adv Technol Ser* **3** (1): 154–162. SPE-24180-PA. https://doi.org/10.2118/24180-PA.

Appendix A—Steady-State Foam Data

In this paper, we focus on data relevant to modeling foam mobility in homogenous porous media. Therefore, we recorded LE data either in the absence of an eruption of a much stronger foam at the core outlet or before this foam eruption started. We did not observe this foam eruption at all in our foam scan with the lowest surfactant concentration (0.037 wt%) and at the lowest total superficial velocity used in our experiments. **Fig. A-1** shows experimental data at one foam quality of this foam scan, where a stronger foam did not erupt at the core outlet even after a prolonged injection period. In this experiment, the pressure gradient is nearly independent of gas expansion along the core, as expected in the high-quality regime. In the high-quality regime, the pressure gradient is nearly independent of gas superficial velocity at fixed liquid superficial velocity (Osterloh and Jante 1992; Alvarez et al. 2001).

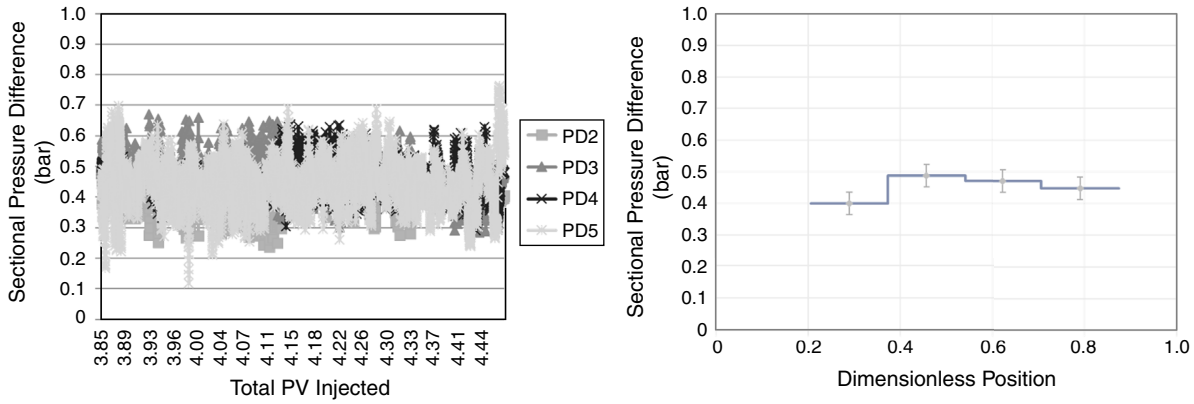

Fig. A-1—(Left) Experimental data of Experiment 1 at fixed foam quality of 90%. (Right) Mean and standard deviation of data in each of the core sections, over the data in the plot on the left between 3.85 and 4.45 PV injected. The mean sectional pressure difference along the four sections (PD2, PD3, PD4, and PD5) is equal to 0.45 bar.

For higher surfactant concentrations and total superficial velocities, we observed eruption of stronger foam at the end of the core at foam breakthrough and subsequent upstream propagation of the stronger foam state, as reported by others (Apaydin and Kovscek 2001; Nguyen et al. 2003; Simjoo et al. 2013). In these cases, the fractional-flow curve based on data at the eventual steady state was not monotonic. In addition, pressure gradient was not uniform along the core, even at high foam qualities expected to reflect the high-quality regime. Therefore, to obtain data free of the effect of the core outlet, in these cases, we used a foam generator to help achieve local equilibrium before foam breakthrough, as confirmed by the following observations. First, the pressure difference in the first section suggests that foam achieves local equilibrium in the core within the first 8 cm, as illustrated in **Fig. A-2.** The pressure gradient is independent of gas superficial velocity (which is altered by gas expansion) along most of the core, as we expect in the high-quality regime. In this paper, we report only data before the eruption of a much stronger foam at the core outlet occurred (before 1 PV in Fig. A-2). We discuss steady-state behavior after foam breakthrough in these cases in a separate paper (Salazar and Rossen 2019; see also Salazar Castillo 2019).

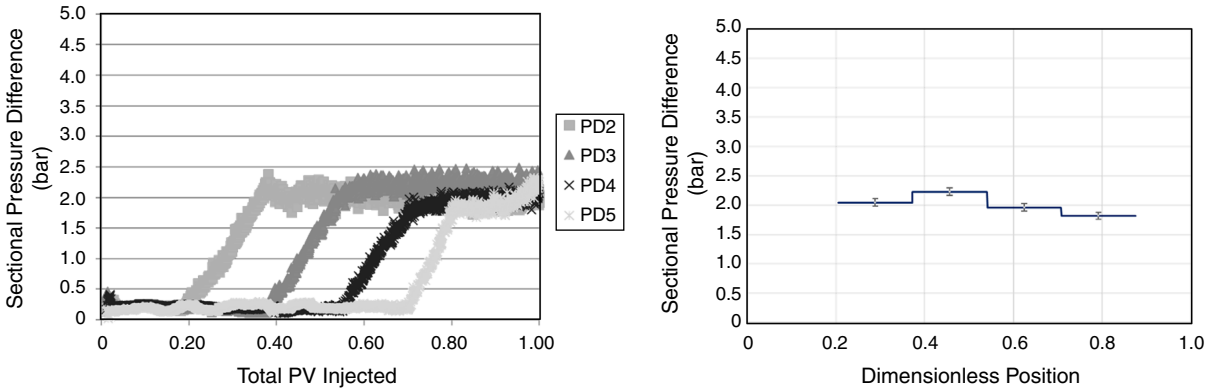

Fig. A-2—(Left) Experimental data for Experiment 4 at a fixed foam quality of 95%. A stronger foam erupts at the core outlet at approximately 1.0 PV. Before this, the pressure gradient is nearly uniform along the core, as expected at local equilibrium in the high-quality regime (Alvarez et al. 2001). (Right) Mean and standard deviation of data in Sections 2 to 5 between 0.8 and 0.9 PV injected, when foam is at local equilibrium in those sections. The mean sectional pressure difference along the four sections (PD2, PD3, PD4, and PD5) is equal to 2.02 bar.

Appendix B—Corey-Brooks Relative-Permeability Model and Foam Model

According to the Corey-Brooks relative-permeability model, the water and gas relative permeabilities are defined as

$$k_{rw} = k^0_{rw} S^{n_w}, \quad \text{(B-1)}$$

$$k_{rg} = k^0_{rg} (1 - S)^{n_g}, \quad \text{(B-2)}$$

$$S \equiv \frac{S_w - S_{wr}}{1 - S_{wr} - S_{gr}}, \quad \text{(B-3)}$$

where k_{rw}, k_{rg}, k^0_{rw}, k^0_{rg}, n_w, n_g, S, S_w, S_{wr}, and S_{gr} denote, respectively, liquid and gas relative permeabilities, the endpoint water and gas relative permeabilities, the water and gas Corey-Brooks exponents, normalized water saturation, and the residual water and gas saturations. **Table B-1** summarizes the two sets of Corey-Brooks parameters used in this study. Kapetas et al. (2017) obtained their set of parameters in the absence of foam and at relatively small pressure gradient, whereas Eftekhari and Farajzadeh (2017) performed a fit on a data set containing both data from coreflood experiments in the presence of foam at different surfactant concentrations (0.03 wt%; AOS, 0.1 wt% AOS; 0.5 wt% AOS, and 0.5 wt% Amphosol) and data from the literature in the absence of foam at a large pressure gradient. We use the parameters of Eftekhari and Farajzadeh (2017) to infer the water-saturation data reported here and to perform the corresponding fits and calculations. We use the Corey-Brooks parameters of Kapetas et al. (2017) to study the impact of using a function that does not reproduce liquid-saturation measurements.

Kapetas et al. (2017)		Eftekhari and Farajzadeh (2017)	
No Surfactant and at Low Pressure Gradients		Range of C_S = 0.03 wt% AOS, 0.1 wt% AOS, 0.5 wt% AOS, and 0.5 wt% Amphosol	
S_{wr} = 0.25	S_{gr} = 0.2	S_{wr} = 0.05	S_{gr} = 0.03
k^0_{rw} = 0.39	k^0_{rg} = 0.59	k^0_{rw} = 0.72	k^0_{rg} = 0.59
n_w = 2.86	n_g =0.7	n_w = 4.42	n_g =0.94

Table B-1—Corey-Brooks parameters used in this study.

In the presence of foam, the STARS model (Cheng et al. 2000; Computer Modelling Group 2015) represents the effect of foam by altering only the gas relative permeability. To model this effect, it incorporates a mobility-reduction factor, *FM,* in the gas phase as follows:

$$u_t f_g = -\frac{k k^f_{rg}}{\mu_g}\nabla P = -\frac{k k_{rg} FM}{\mu_g}\nabla P, \quad \text{(B-4)}$$

where $u_t, f_g, k, k_{rg}, k^f_{rg}, \mu_g$, and ∇P denote, respectively, total superficial velocity, quality (gas fractional flow), permeability, gas relative permeability in the absence and presence of foam, respectively, gas viscosity, and pressure gradient.

The mobility-reduction factor, *FM,* models the effects of surfactant concentration, water saturation, oil saturation, gas velocity, capillary number, and the critical capillary number, respectively, on gas mobility. Here we focus on the dependence on water saturation (and, by implication, on capillary pressure) through the function F_2, which controls behavior in the high-quality regime. For a fit to an entire foam scan, including the low-quality regime, it is essential to include also the dependence on capillary number through the function F_5, which is important in that regime. Otherwise, to fit data in this regime, the model distorts the value of *epdry,* which is important in the high-quality regime as well (cf. Farajzadeh et al. 2015). In that case, the mobility-reduction factor becomes

$$FM = \frac{1}{1 + fmmob\ F_2\ F_5}, \quad \text{(B-5)}$$

where the parameter *fmmob* is the reference gas mobility-reduction factor for wet foams.

F_2, also known as the dry-out function, models the abrupt collapse of foam produced by the limiting capillary pressure at a characteristic water saturation value (*fmdry,* in the STARS) with the following expression:

$$F_2 = \left\{0.5 + \frac{\arctan[epdry(S_w - fmdry)]}{\pi}\right\}, \quad \text{(B-6)}$$

where *epdry* controls the abruptness of the transition. This model does not incorporate foam collapse at irreducible water saturation S_{wr}. If we further assume complete foam collapse at S_{wr}, we add the NZ modification (Namdar Zanganeh et al. 2014). In this case, the expression for F_2 is

$$F_2 = \left\{0.5 + \frac{\arctan[epdry(S_w - fmdry)]}{\pi}\right\} - \left\{0.5 + \frac{\arctan[epdry(S_{wr} - fmdry)]}{\pi}\right\}, \quad \text{(B-7)}$$

where the second term forces a complete foam collapse, making $F_2 = 0$ at S_{wr}.

The F_5 function models shear-thinning rheology in the low-quality regime through the parameters *epcap* and *fmcap* as follows:

$$F_5 = \begin{cases} \left(\dfrac{fmcap}{N_{ca}}\right)^{epcap} & \text{if } N_{ca} > fmcap \\ 1 & \text{any other case,} \end{cases} \quad \text{(B-8)}$$

where the parameter *fmcap* acts as a reference capillary number, and the parameter *epcap* is related to the power law exponent, *n,* by $n \approx 1/(1 + epcap)$. Here, the capillary number for foam is defined as $N_{ca} = (k\nabla P)/\sigma_{wg}$, where σ_{wg} denotes the surface tension between the aqueous and gas phases.

In the high-quality regime that dominates SAG processes, the shear-thinning behavior of the low-quality regime is not important. Because in the model, F_5 is bounded at 1 for $N_{ca} < fmcap$, one must set *fmcap* to a value at least as small as the smallest value of N_{ca} expected to be encountered in a given simulation (Boeije and Rossen, 2015a). This in turn alters the value of *fmmob* in the fit. To correct for this alteration in the value of *fmmob* while excluding F_5 in the scaleup for SAG, we replace the value of *fmmob* from the model fit with the product of the fitted value of *fmmob* and the value of F_5 that applies in the range of the pressure gradient of the laboratory data, particularly at the tangency condition that governs the gas-injection process of the first slug. Let this value of F_5 that applies approximately in the vicinity of the point of tangency be F'_5 (a constant). We denote this new *fmmob* as $fmmob_{SAG}$:

$$fmmob_{SAG} = F'_5\ fmmob \quad \text{(B-9)}$$

For the scaleup of SAG data, we drop the F_5 factor from Eq. B-4 and we replace *fmmob* with $fmmob_{SAG}$.

Appendix C—Dimensionless Injection Pressure as Function of Dimensionless Time

We scale up our parameters to a hypothetical field application, assuming that the reservoir is cylindrical and homogenous with inner radius $r_w = 0.1$ m and outer radius $r_e = 100$ m, where the outer boundary is open. We define the dimensionless pressure, P_D, as the ratio of the pressure rise needed to inject gas into a fully surfactant-saturated reservoir to the pressure needed to inject water into the same fully liquid-saturated reservoir at the same volumetric injection rate Q. We calculate the pressure difference between the wellbore and the outer radius by integrating $\nabla P(r)$ between r_w and r_e (Al Ayesh et al. 2017; Salazar Castillo et al. 2020). Assuming a water viscosity of 0.001 Pa·s, the expression for P_D is

$$P_D = \frac{\int_{r_w}^{r_e} \frac{1}{r\lambda_{rt}(S_w)} dr}{\frac{1}{1,000} \times \ln\left(\frac{r_e}{r_w}\right)}, \quad \text{(C-1)}$$

where $\lambda_{rt}(S_w)$ denotes the total relative mobility of each characteristic. We compute the integral numerically using 300 characteristics equally spaced in saturation from the point of tangency to S_{wr}. **Fig. C-1** illustrates the evolution of P_D during the injection of the first gas slug in a surfactant-saturated reservoir for the foam of Experiment 4 for the different fits explored here. In all cases, P_D increases abruptly and remains nearly constant until foam breaks through the outer radius (Boeije and Rossen 2015b).

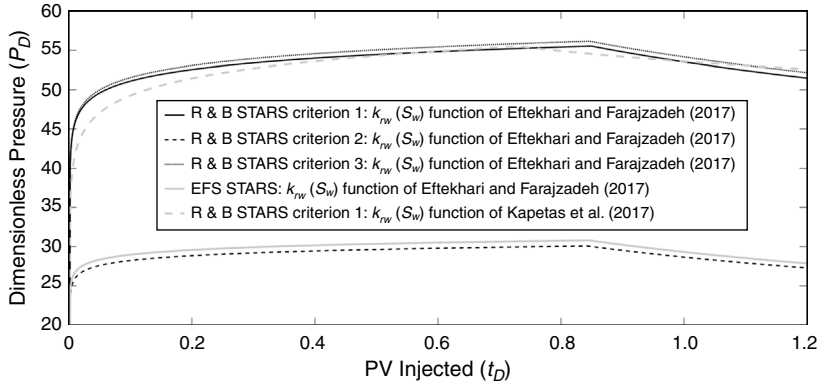

Fig. C-1—Injectivity for different fits for the data of Experiment 4. We use the foam scan data corresponding to Experiment 4. The corresponding foam parameters and mobilities behind the shock are listed in Tables 1, 3, and 4.